Chirality in Topologically Interlocked Material Systems

Dong Young Kim, Thomas Siegmund(1)

School of Mechanical Engineering, Purdue University, West Lafayette, IN 47907, USA;
(1) Corresponding Author, siegmund at purdue.edu

Abstract

The present study focuses on the mechanical chirality in plate-type topologically interlocked material systems. Topologically interlocked material (TIM) systems are a class of dense architectured materials for which the mechanical response emerges from the elastic behavior of the building blocks and the contact-frictions interactions between the blocks. The resulting mechanical behavior is strongly non-linear due to the stability-instability characteristics of the internal load transfer pattern. Two tessellations are considered (square and hexagonal) and patches from each are used as templates. While individual building blocks are achiral, chirality emerges from the assembly pattern. The measure of *microstructure circulation* is introduced to identify the geometric chirality of TIM systems. TIM systems identified as geometrically chiral are demonstrated to possess mechanical chiral response with a force-torque coupling under transverse mechanical loading of the TIM plate. The chiral length is found to be constant during the elastic response, yet size-dependent. During nonlinear deformation, the chiral length scale increases significantly and again exhibits a strong size dependence. The principle of dissection is introduced to transform non-chiral TIM systems into chiral ones. In the linear deformation regime, the framework of chiral elasticity is shown to be applicable. In the non-linear deformation regime, chirality is found to strongly affect the mechanical behavior more significantly than in the linear regime. Experiments on selected TIM systems validate key findings of the main computational study with the finite element method.

Keywords: Architectured Material Systems, Chirality, Circulation, Length Scales, Mechanical Properties

1. Introduction

There is distinct evidence that deformation and failure behavior of materials can require the consideration of internal and emerging length scales [1, 2, 3, 4]. Chiral materials are one type of materials in which a length scale is present. Architectured materials and material systems [5] present themselves as opportunities to realize mechanical chirality. Chiral cellular architectured materials with chiral mechanical behavior are constructed from either re-entrant, rotating, or chiral unit cells [6, 7, 8, 9, 10, 11]. Chiral kirigami [12] and tile structures [13] are based on the rotation of gaps in the microstructure. Dense chiral architectured materials are composites with chiral seciond phases [14, 15] or specific spatial orientation and distribution of phases [16, 17].

This present study investigates chirality in Topologically Interlocked Material (TIM) systems [18]. In TIM systems, polyhedra are arranged in an overall planar configuration such that neither building block can be removed from the assembly without disassembly of the overall system. The most fundamental such assembly is the densest packaging of tetrahedra in a plane [19]. Once the assembly is confined by a bounding frame, the assembly can carry transverse loads, much like a plate [20, 21, 22]. Contact and friction then determine the mechanical load response and, similar, to granular solids, lead to the formation of an internal force chain system. The deflection behavior of 2D TIM systems can be described by a theory expanding on concepts of the Mises truss structure and its instability [23]. TIM systems are of relevance in the context of brittle solids as contact interfaces act as crack arrestors and alter failure probabilities [20] and increase toughness compared to monolithic constructs, particularly when considering brittle materials. The optimized selection of building block geometry and the characteristics of interaction block-to-block interaction can allow for the construction of TIM systems that exceed both the toughness and the strength of the monolithic counterpart [24]. We address the following questions.

- We seek to determine how chirality emerges in a TIM system where individual building blocks are not chiral. We expect chirality in TIM systems to be an emerging property connected to the building block geometry and the assembly pattern, similar to [13, 25, 26].

- If the assembly structure and building block geometry define chirality, can microstructure descriptors of chirality in TIM systems be defined?

2

If so, how does such a geometric descriptor relate to the mechanical response?

- The main focus of past investigations on mechanical chirality relates to investigations of the elastic response and the definition of constitutive relations allowing for rotations and moments in addition to stress and strain. TIM systems uniquely allow for the investigation of the chiral response throughout the initial elastic, nonlinear deformation, and damage regimes. We seek to determine how the chiral character changes throughout these domains of deformation. This will allow us to assess effects related to internal length scales on strength and toughness.

- Finally, we seek to expand the design space for chiral TIM systems. While the theory of tessellation provides the templates for the construction of TIM systems, uniform tessellations have limitations in achieving variations solely through the arrangement of tiles. Yet additional variation of the tessellation pattern can be realized using the principle of dissection, [27]. We seek to determine how the principle of dissections can be used to modulate the chirality in TIM systems.

We address these questions by the use of computational modeling and experiments.

2. Methods

2.1. Tessellation Pattern

The mid-plane section of a TIM system is a 2D tessellation that serves as the starting point for the design of a TIM system. The uniform square and uniform hexagon tessellations provide the baseline templates. Tessellation patterns are further modulated by the applications of principles of dissection.

2.1.1. Patches with a Single Prototile

For square tessellations, patches with two types of configuration at the patch center are possible [28]. For patches $\mathcal{S}_1(i)$, the patch center is at the center tile of the patch, Fig. 1(a-d). These square patches possess an odd-numbered tile count, $i = 3, 5, 7, 9, ...$, at each edge. For square patches $\mathcal{S}_2(i)$ the center is at the intersection of four tiles, Fig. 1(e-h). These patches

possess an even-numbered tile count, $i = 4, 6, 8, ...$, along each edge. We consider $3 \leq i \leq 10$. The number of tiles N in patches $\mathcal{S}_1(i)$ and $\mathcal{S}_2(i)$ is:

$$N^{\mathcal{S}_1} = N^{\mathcal{S}_2} = i^2 \tag{1}$$
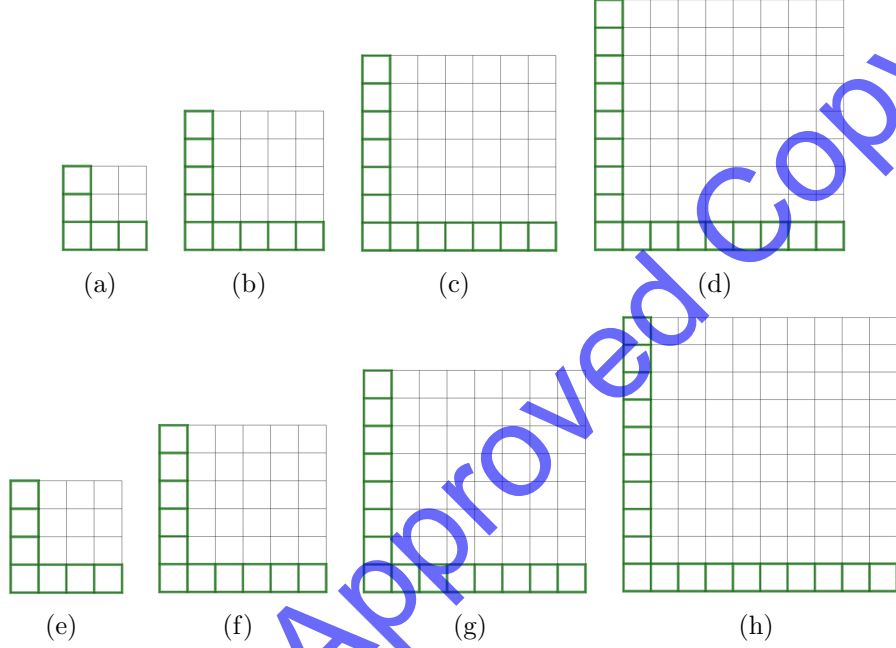

Figure 1: Patches of square tiles: (a-d) $\mathcal{S}_1$: $i = 3, 5, 7, 9$; (e-f) $\mathcal{S}_2$: $i = 4, 6, 8, 10$.

For hexagonal tiles, two types of patches are considered, Fig. 2 [28]. For patches $\mathcal{H}_1(i)$, Fig. 2(a-d), the patch center is at the center tile. For patches $\mathcal{H}_2(i)$, Fig. 2(e-h), the center point is situated at the intersection of three tiles. We consider consider $2 \leq i \leq 5$. The number of tiles N in $\mathcal{H}_1$ and $\mathcal{H}_2$, respectively, is:

$$N^{\mathcal{H}_1} = 3i^2 - 3i + 1 \tag{2}$$
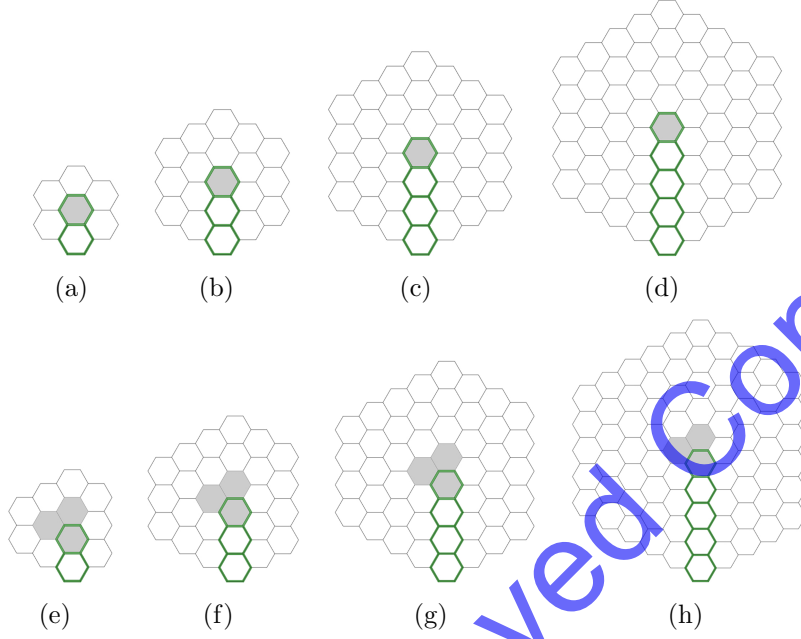$$N_i^{\mathcal{H}_2} = 3i^2 \tag{3}$$

4

Figure 2: Patches of hexagonal tiles: (a-d) $\mathcal{H}_1$: $i = 2, 3, 4, 5$; (e-f) $\mathcal{H}_2$: $i = 2, 3, 4, 5$.

Figure 3 depicts the interlocking building block geometry for square and hexagon tiles. The edge length of the square is a_0. Square and hexagonal prototiles areas, A_s and A_h, respectively, are set to be identical $a_0^2 = A_S = A_H$. We construct interlocking building blocks by projecting each edge of the tiles at alternating angles $|\varphi| = 17°$, and terminate the tilted side faces to a block height $h/a_0 = 0.5$.

5

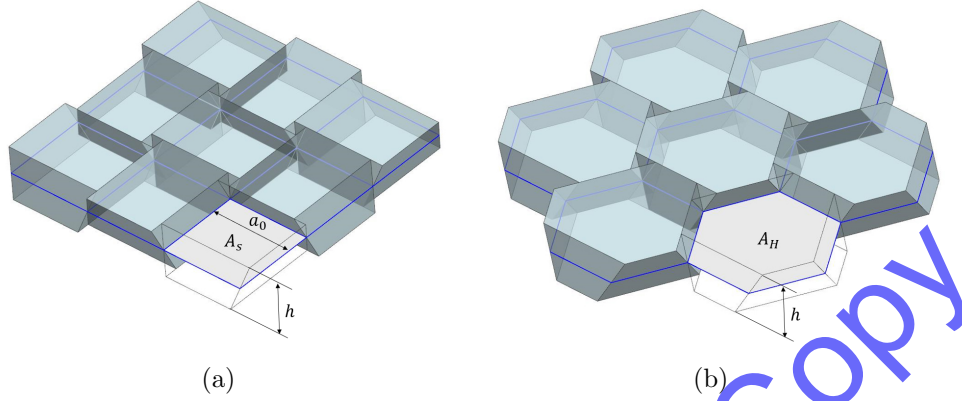Figure 3: Assemblies of interlocking building blocks (thickness h, square edge length a_0, mid-section area $a_0^2 = A_{\mathcal{S}} = A_{\mathcal{H}}$ for patches of type (a) $\mathcal{S}$ and (b) $\mathcal{H}$.

2.1.2. Patches with Dissections

A dissection provides a collection of polygons that can be arranged to form the original tile of interest. In a TIM system, every building block possesses inclined side faces with alternating inclinations toward and away from the normal direction to the tessellation plane. Thus, all polygons in the tessellation and its dissections must possess an even number of sides so that a complete set of matching inclinations is enabled. Also, tile vertices must be matched with other tile vertices.

A Haberdasher's puzzle [29] visualizes this constraint, Fig. 4. Accordingly, a typical dissection of the triangle, Fig. 4(a), to transform to a square, Fig. 4(b), is not suited here. This dissection contains triangles, e.g. $\overline{\text{HIF}}$ as well as edge-matched vertices, e.g. vertex A on $\overline{\text{HI}}$.
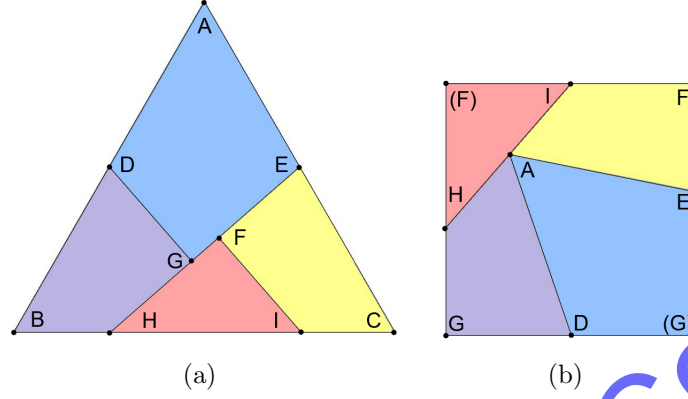
Figure 4: Haberdasher's puzzle to demonstrate the principle of dissection: (a) triangle-to-(b) square dissection.

The Penrose tessellation [30] provides rules for allowable dissections of quadrilaterals [31]. Figure 5(a) shows a kite-dart configuration for a Penrose-type tessellation on a parallelogram. For the square tessellations here, the angles of the dissecting lines are modified from those in the Penrose-type tessellation $(36°, 72°)$ to $(30°, 60°)$. The resulting dissection, Fig. 5(b), can be used to construct building blocks allowing for the assembly of a TIM system, Fig. 5(c). The dissection of hexagons into rhombuses [32] provides rules for allowable dissections for the hexagon tessellations, Fig. 6(a). The three resulting building blocks are presented in Fig. 6(b).
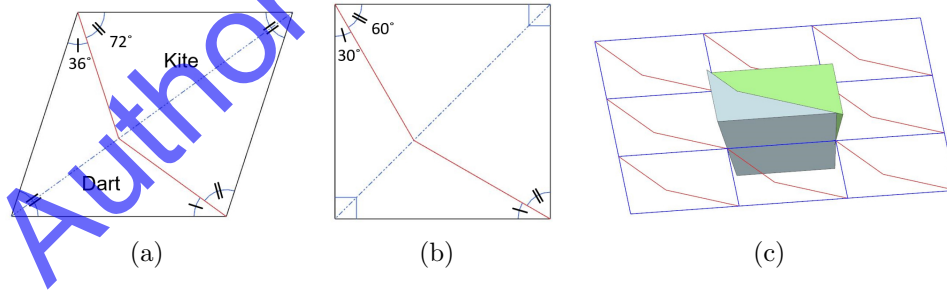

Figure 5: (a) Kite-dart configuration in the Penrose tessellation, (b) modified kite-dart configuration for the square tile, (c) building blocks for the dissected square tile.
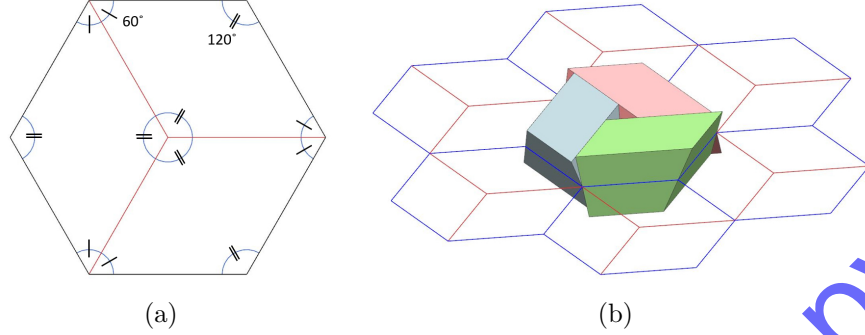
Figure 6: (a) Hexagon tile dissected into three rhombus tiles, (b) building blocks for the dissected hexagon tile.

2.2. Architecture Descriptor

The directions of alternating angles of tile faces, Figs 7(a) and 7(b), play a central role in the load transfer mechanism in TIM systems as load transfer follows the angle direction [33]. We represent the projection direction of a plane by its plane tilt vector $\vec{t}$. Considering the center tiles in Figs 7(a) and 7(b), red-colored planes are tilted inward, and the respective vector points to the tile center; blue-colored planes are tilted outward and the respective tilt vector points away from the tile. By representing these tilt vectors across the entire TIM system, a field of $\vec{t}$ is obtained.

Chirality is defined as a directional property, i.e. right/left-handedness. We define chirality of the architecture of the TIM systems as the circulation, C, of the tilt vector field $\vec{t}$ by integrating along a closed loop L centered at the patch center:

$$C = \oint_L \vec{t} \, d\vec{r} \tag{4}$$

where $d\vec{r}$ is tangential along L. The condition $C = 0$ defines an *achiral* architecture while $C \neq 0$ defines a *chiral* architecture (counter-clockwise or clockwise). In this study, only cases with $C > 0$ are considered.
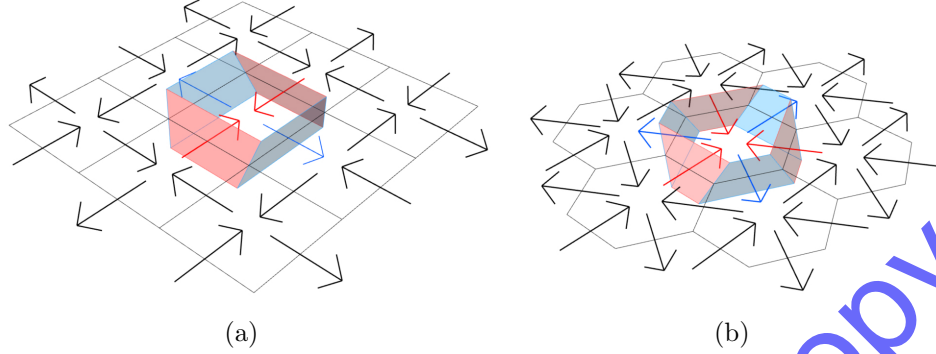
8

Figure 7: Tessellations and projected side planes in a (a) square and (b) hexagon tessellation. Tilt angles are expressed by the tilt vector field $\vec{t}$.

2.3. Computational Methods

We employ finite element analysis for the numerical simulations of the mechanical response of the TIM systems. Building blocks are linear elastic solids, with properties of the polymer in the experimental part of the study (modulus E=1.827 GPa and Poisson's ratio ν=0.35). A linear pressure-overclosure relationship defines the normal interaction between building blocks. The contact stiffness is $K = 100,000E/l_0$, in order to limit contact overclosure value, with l_0 being unit length. The tangential interaction is given by a Coulomb friction model and a coefficient of friction of μ=0.3. A patch of building blocks is confined within an external frame with matching geometry. The TIM systems are constrained against axial rotation ($\theta_z = 0$). A centrally positioned indentor provides a transverse mechanical load to the TIM systems. The indenter is modeled as a rigid body.

The indenter prescribes a normalized transverse deflection δ/h and is constrained against axial rotation ($\theta_z = 0$). The normalized force in the indenter axis, $F/(EH^2)$, and normalized moment about the indenter axis, $M/(Eh^3)$, are calculated from data computed at the reference point of the indenter part. Consequently, force-displacement and moment-displacement records are obtained. We quantify chirality the normalized chiral length, L_c/h obtained as the ratio of the normalized moment to normalized force.

The bounding frame is created by adding an additional layer of building blocks on each edge and by fusing the additional blocks into one rigid body. A mass-scaled dynamic FE approach is used (ABAQUS/Explicit) as the interest is in the long-term, quasi-static response of the system. Mass

density was set such that the kinetic energy component in the system solution remains a small fraction of the other energy components throughout the analysis. The applied displacement function is sigmoidal to a constant velocity of $\dot{\delta}/h = 10.0$ /s. Computational files are available [34].

2.4. Experimental Methods

We manufactured physical realization of TIM systems for patches $\mathcal{S}_1(i = 3)$, $\mathcal{S}_2(i = 4)$, $\mathcal{H}_1(i = 2)$, and $\mathcal{H}_2(i = 2)$, Fig. 1 and Fig. 2. We also manufacture a dissected variant of $\mathcal{H}_1(i = 2)$, i.e. $\mathcal{H}_1^{\mathrm{d}}(i = 2)$. The assemblies of individual building blocks are confined by matching bounding frames. The TIM systems are created using a Stratasys Objet 350 Polyjet 3D Printer. Individual building blocks ($h = 5.0$ mm and $a_0 = 10.0$ mm) and the bounding frames are printed with the polymer resin VeroWhitePlus. After the print process, the support resin is removed. A consistent assembly method is provided. First, all building blocks are positioned in accordance with the patch under consideration. Then, a two-part configuration of the bounding frame is placed to surround the assembly. An elastic rubber band is stretched along the outside of the frame parts and constrains the assembly. The length of the rubber band is selected to minimize the pre-stress in the assembly. Assembly conditions between patches are controlled by ensuring equal strain in the rubber band for all assemblies built. Adhesive bonding is applied at the joints of two two-part frames to merge the frames into a single part to constrain the patch, and the rubber band is removed, Fig. 8(a).

Patches are subjected to a transverse uniaxial displacement applied at the center of the patch. The specimens and the indenter are constrained against rotation, $\theta_z = 0$. The displacement, δ is applied through a cylindrical indenter of diameter 6.0 mm ($\dot{\delta} = 2.0$ mm/min). Both the axial reaction force F and the reaction moment around the load axis M are measured in dependence on δ. The chiral length is $L_c = M/F$. The experimental set-up is depicted in Fig. 8(b). The assembly is inserted in a holder attached to a digital moment gauge (ATGE05CN-G). The torque gauge is located in the load axis of a uniaxial test machine (TESTRESOURCES, 100 load frame) with the indenter attached to the load cell.
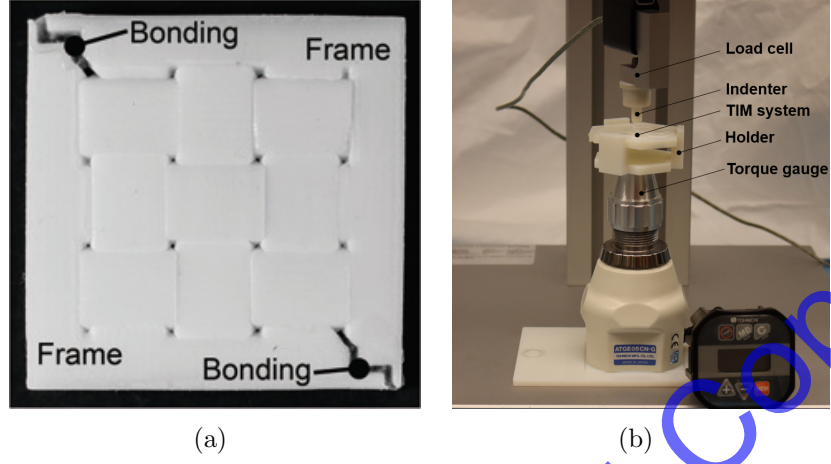
10

Figure 8: (a) Example of patch used in the experiments, $\mathcal{S}_1(i = 3)$: building block assembly as constrained by a two-part bounding frame joined by adhesive bonding. (b) Transverse point deflection experiment with measurement of reaction F and M.

3. Results

3.1. Architecture and Chirality

Figure 9 shows the tilt vector fields $\vec{t}$ for patches $\mathcal{S}_1(i = 3)$ and $\mathcal{S}_2(i = 4)$ together with the loop L closest to the loading point. Circulation C is evaluated following Eq. 4 as $C = \sum_i \vec{t}_i \cdot \vec{r}_i$. For $\mathcal{S}_1(i = 3)$, and similar other odd-numbered patches, Fig. 9(a), $C = 0$. Patches $\mathcal{S}_1$ are achiral. For $\mathcal{S}_2(i = 4)$ and similar other even-numbered patches, Fig. 9(b), $C > 0$. Patches $\mathcal{S}_2$ are chiral with a counter-clockwise rotation. Figure 10 depicts $\vec{t}$ and L for $\mathcal{H}_1(i = 2)$ and $\mathcal{H}_2(i = 2)$. Patches $\mathcal{H}_1$, $C = 0$, these patches are achiral. For patches $\mathcal{H}_2$, $C > 0$, these patches are chiral, again with a counter-clockwise rotation.
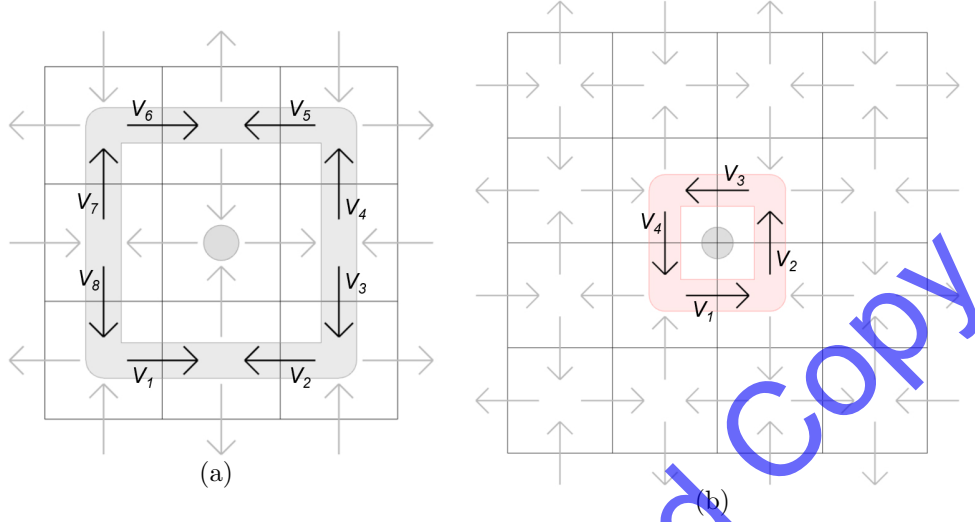
11

Figure 9: Tilt vectors $\vec{t}$ and loop L to determine the circulation in (a) $\mathcal{S}_1(i=3)$ and (b) $\mathcal{S}_2(i=4)$. Circulation: gray - achiral, red - chiral.
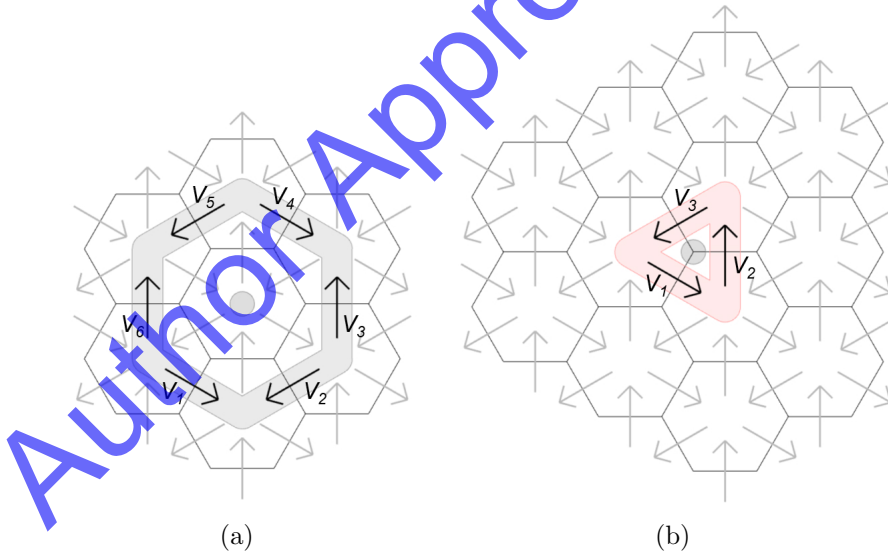

Figure 10: Tilt vectors $\vec{t}$ and loop L to determine the circulation in (a) $\mathcal{H}_1(i=2)$ and (b) $\mathcal{H}_2(i=2)$. Circulation: gray - achiral, red - chiral.

Figure 11 depicts $\vec{t}$ and L for the uniform patches $\mathcal{S}_1(i=5)$ and $\mathcal{S}_2(i=6)$ and their dissection $\mathcal{S}_1^{\mathrm{d}}(i=5)$, $\mathcal{S}_1^{\mathrm{D}}(i=5)$, and $\mathcal{S}_2^{\mathrm{d}}(i=6)$. The uniform patch

12

$\mathcal{S}_1$ is achiral ($C = 0$), Fig. 11(a). With the dissection of the center building block as shown in Fig. 11(b), the patch $\mathcal{S}_1^{\mathrm{d}}$, however, possesses $C > 0$, and becomes chiral. Alternatively, the dissections of six building blocks in the layer surrounding the center tile of $\mathcal{S}_1$, leads to $\mathcal{S}_1^{\mathrm{D}}(i = 5)$, Fig. 11(c) also with $C > 0$. Patches $\mathcal{S}_2$ are chiral even for the initial achiral uniform tessellation, Fig. 11(d). The dissection of the building blocks at the patch center leads to $\mathcal{S}_1^{\mathrm{d}}(i = 6)$, Fig. 11(e) which retains $C > 0$.
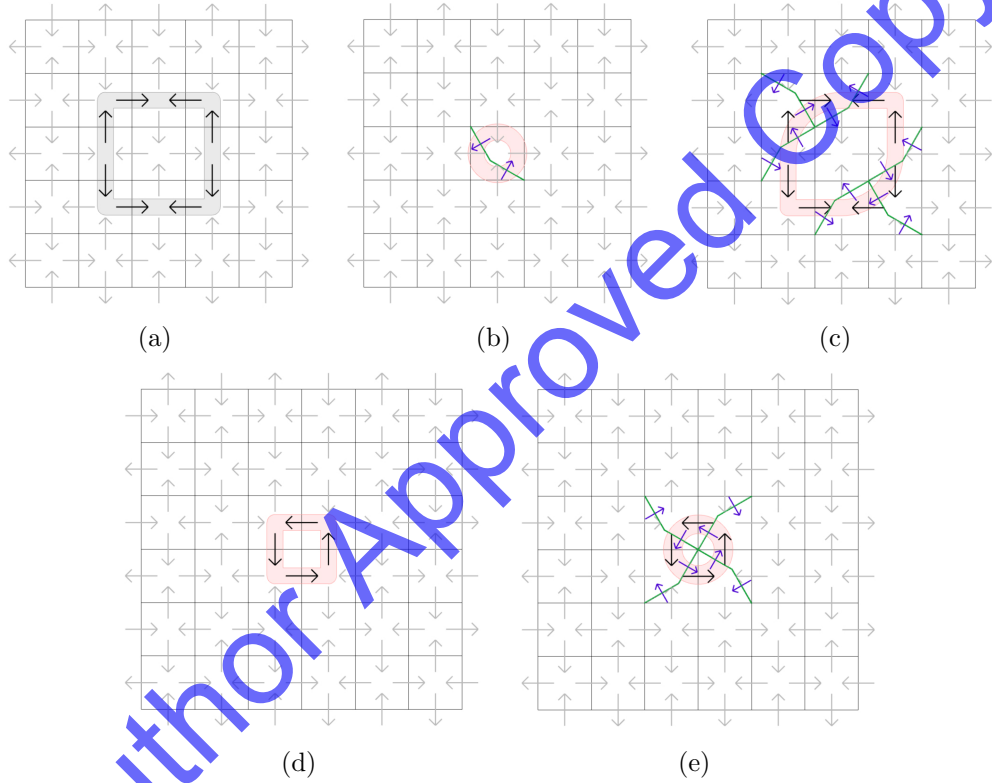

Figure 11: Tilt vectors $\vec{t}$ and loop L to in the presence of dissection: (a) no dissection: $\mathcal{S}_1(i = 5)$, (b) center dissection: $\mathcal{S}_1^{\mathrm{d}}(i = 5)$, (c) center-surround dissection: $\mathcal{S}_1^{\mathrm{D}}(i = 5)$, (d) no dissection: $\mathcal{S}_2(i = 6)$, (e) center dissection: $\mathcal{S}_2^{\mathrm{d}}(i = 6)$. Circulation: gray - achiral, red or blue - chiral.

Figure 12 depicts $\vec{t}$ and L for the original patches $\mathcal{H}_1(i = 3)$ and $\mathcal{H}_2(i = 3)$ and their dissections $\mathcal{H}_1^{\mathrm{d}}(i = 3)$, $\mathcal{H}_1^{\mathrm{D}}(i = 3)$, and $\mathcal{H}_2^{\mathrm{d}}(i = 3)$. The uniform patch $\mathcal{H}_1(i = 3)$ is achiral, Fig. 12(a). With the dissection of the center building block, we introduce the patch $\mathcal{H}_1^{\mathrm{d}}(i = 3)$ as shown Fig. 12(b). This

13

patch is chiral, $C > 0$. With the dissections applied to the six building blocks surrounding the center tile we obtain $\mathcal{H}_1^{\mathrm{D}}(i = 3)$ as shown Fig. 12(c). This patch is again chiral, $C > 0$. The uniform patch $\mathcal{H}_2(i = 3)$ is chiral, Fig. 12(d), and the dissection of the building blocks at the patch center leads to $\mathcal{H}_2^{\mathrm{d}}(i = 3)$ as shown in Fig. 12(e) which retains $C > 0$.
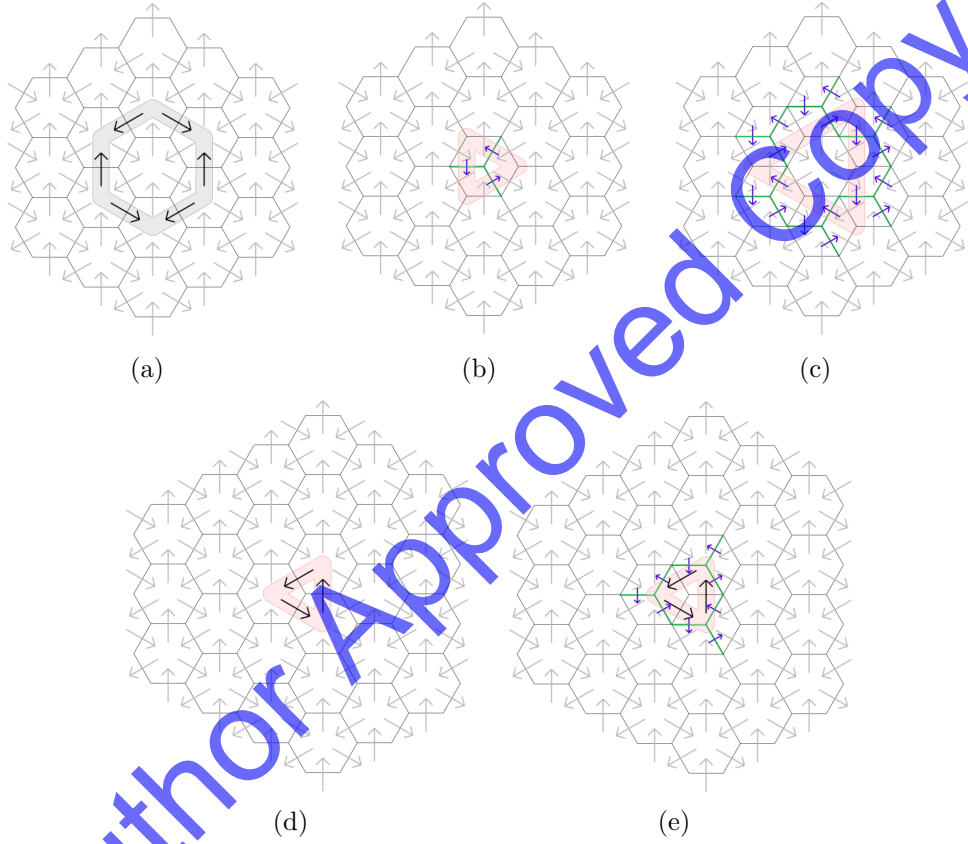

Figure 12: Tilt vectors $\vec{t}$ and loop L in the presence of dissection: (a) no dissection: $\mathcal{H}_1(i = 3)$, (b) center dissection: $\mathcal{H}_1^{\mathrm{d}}(i = 3)$, (c) center-surround dissection: $\mathcal{H}_1^{\mathrm{D}}(i = 3)$, (d) no dissection $\mathcal{H}_2(i = 3)$, (e) center dissection: $\mathcal{H}_2^{\mathrm{d}}(i = 3)$. Circulation: gray - achiral, red or blue - chiral.

3.2. Computational Analysis of Mechanical Behavior

Figure 13 shows data for the mechanical response of one selected TIM system, i.e. $\mathcal{H}_2(i = 3)$ with $C > 0$. The normalized force, $F/(Eh^2)$, - displacement, δ/h, response is typical of the mechanical behavior documented

14

for TIM systems. The $F/(Eh^2)$-δ/h record is parabolic, with maximum load at $\delta/h \approx 0.7$ and final failure at $\delta/h \approx 1.5$. However, there is also a non-zero reaction moment, $M/(Eh^3)$, in addition to the reaction force, Fig. 13(b). Initially, the magnitude of M increases proportional to F. Following $\delta/h > 0.7$, while F starts to decline, M increases at a rate larger than in the initial stages of loading until a maximum in M is reached at about $\delta/h \approx 1.1$. Subsequently, M also drops and reaches zero at $\delta/h \approx 1.5$. The (normalized) chiral length $M/(Fh) = L_c/h$ is found to be significantly different in the initial elastic and subsequent nonlinear deformation regimes, Fig. 13(c). During the initial (reversible) load stage, $\delta/h > 0.4$, $L_c/h = const$. The strength of the chiral response subsequently increases during the nonlinear deformation regime. At the maximum of F, the magnitude of L_c/h is about double its value in the elastic regime. A more significant increase of L_c/h occurs during the subsequent softening response of the axial load such that the maximum value of L_c/h is about seven times that of the elastic regime. In the range following the maximum for the moment, and as the TIM system disintegrates, L_c/h drops to zero.
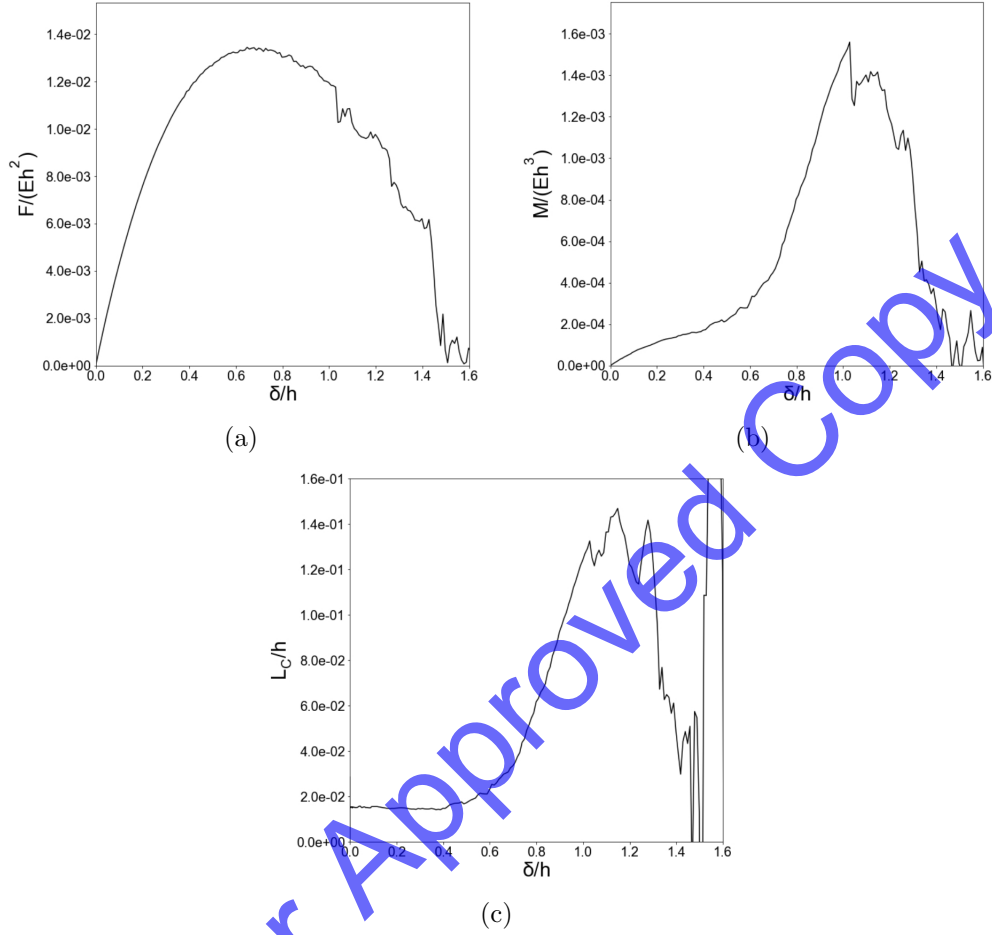
Figure 13: Computed (a) Normalized force, $F/(Eh^2)$, vs. deflection, δ/h, (b) Normalized moment, $M/(Eh^3)$, vs. deflection, δ/h, (c) Normalized chiral length, L_c/h, vs. deflection δ/h for the chiral TIM system $\mathcal{H}_1(i=3)$.

Figure 14 depicts the computed mechanical response of TIMs systems $\mathcal{S}_1$ where $C = 0$. All TIM systems $\mathcal{S}_1$ exhibit the characteristic skew parabolic $F - \delta$ responses. Stiffness, the maximum load, and toughness decline as i is increased. Moments are effectively zero. On the other hand, TIM systems $\mathcal{S}_2$ with $C > 0$ display both axial force and moments, Fig. 15(a,b) and $L_c/h \neq 0$, Fig. 15(c). The chiral response in the elastic regime is found to be dependent on the system size, i, with smaller systems possessing larger chiral length scale. Smaller systems exhibit a more significant relative increase in L_c/h in the nonlinear regime. However, the maximum value of L_c/h is found
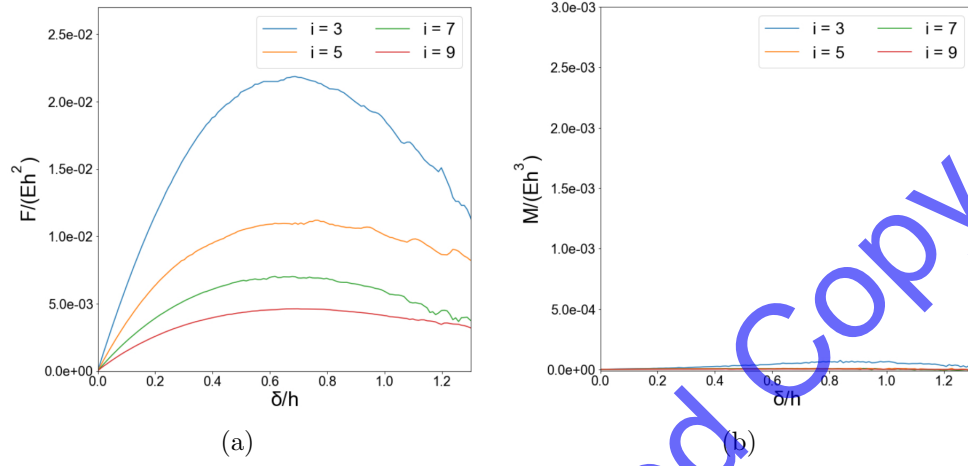
16

as largely independent of the system size.

Figure 14: Computational analysis of TIM systems S_1. (a) Normalized force, $F/(Eh^2)$, vs. deflection, δ/h, (b) Normalized moment, $M/(Eh^3)$, vs. deflection, δ/h.
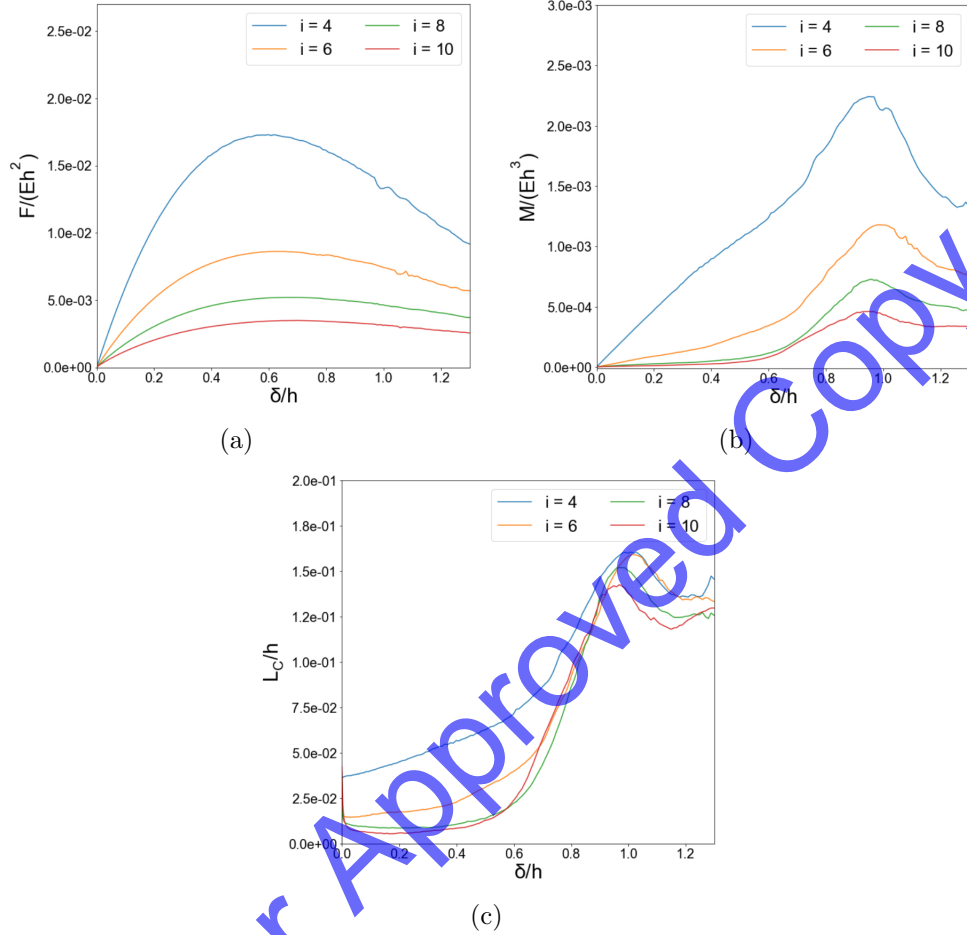
Figure 15: Computational analysis of TIM systems type $\mathcal{S}_2$. (a) Normalized force, $F/(Eh^2)$, vs. deflection, δ/h, (b) Normalized moment, $M/(Eh^3)$, vs. deflection, δ/h, (c) Normalized chiral length, L_c/h, vs. deflection δ/h.

Figure 16 depicts the computed mechanical properties of the achiral hexagonal TIM systems $\mathcal{H}_1$. The $F - \delta$ response exhibits the typical skewed parabolic character, 16(a), but moments are found to be absent, Fig. 16(b). However, the chiral hexagonal TIM systems $\mathcal{H}_2$ exhibit both axial forces, Fig. 17(a), and moments, Fig. 17(b) and $L_c/h > 0$, Fig. 17(c). Again, L_c/h is constant in the initial elastic regime and declines with the increase in system size. Again, L_c/h increases during non-linear deformation with the relative increase larger for small system sizes. The maximum values of L_c/h are rather size-independent.
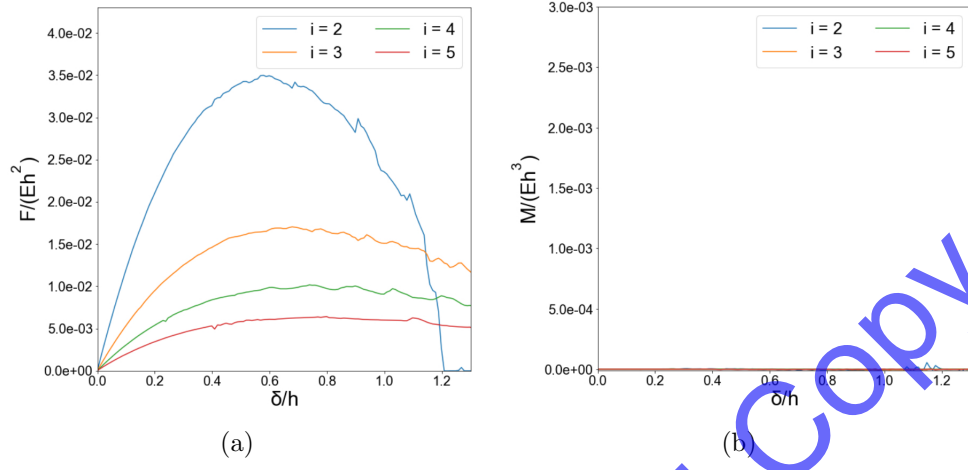
18

(a)

(b)

Figure 16: Computational analysis of TIM systems type $\mathcal{H}_1$. (a) Normalized force, $F/(Eh^2)$, vs. deflection, δ/h, (b) Normalized moment, $M/(Eh^3)$, vs. deflection, δ/h.
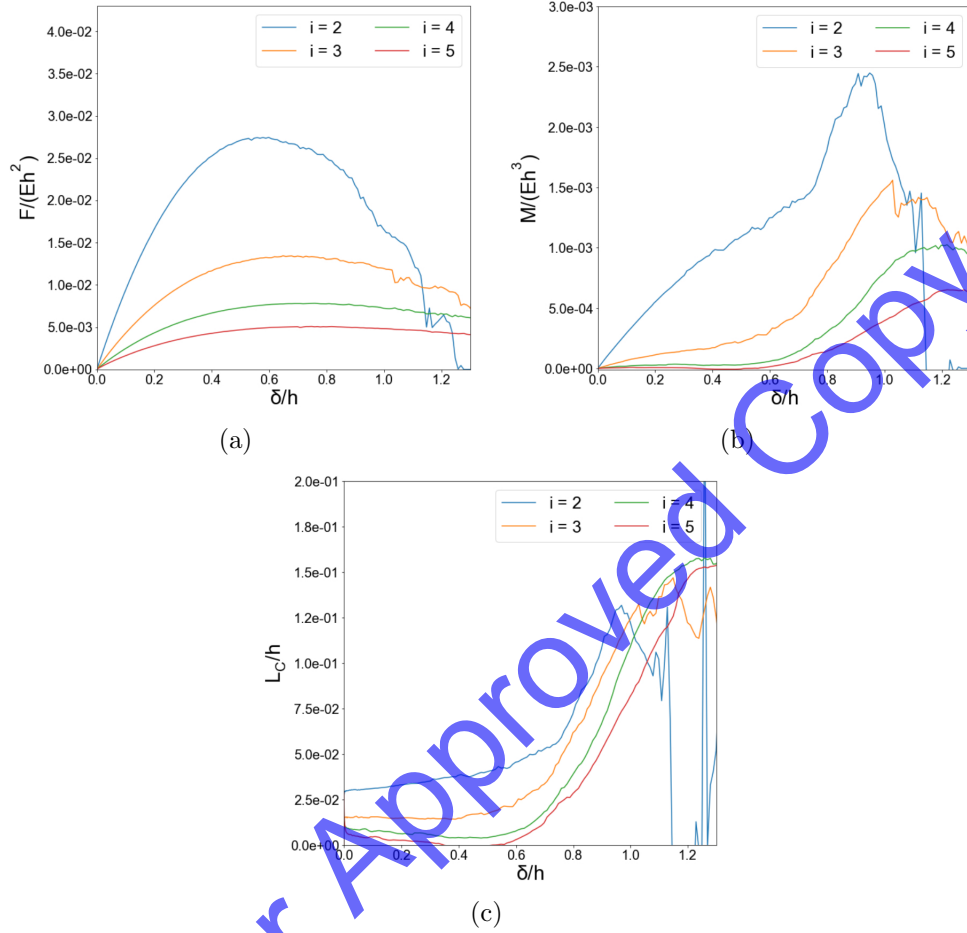
19

Figure 17: Computational analysis of TIM systems type $\mathcal{H}_2$. (a) Normalized force, $F/(Eh^2)$, vs. deflection, δ/h, (b) Normalized moment, $M/(Eh^3)$, vs. deflection, δ/h, (c) Normalized chiral length, L_c/h, vs. deflection δ/h.

The computed response of TIM systems with dissections $\mathcal{S}_1^{\mathrm{d}}(i = 5)$, $\mathcal{S}_1^{\mathrm{D}}(i = 5)$, and $\mathcal{S}_2^{\mathrm{d}}(i = 6)$, Fig. 11, and of $\mathcal{H}_1^{\mathrm{d}}(i = 3)$, $\mathcal{H}_1^{\mathrm{D}}(i = 3)$, and $\mathcal{H}_2^{\mathrm{d}}(i = 3)$, Fig. 12, are depicted in Fig. 18 and Fig. 19, respectively, and compared to those of the original undissected configurations. While the uniform TIM systems $\mathcal{S}_1(i = 5)$ is achiral, both types of dissections, $\mathcal{S}_1^{\mathrm{d}}(i = 5)$ and $\mathcal{S}_1^{\mathrm{D}}(i = 5)$, exhibit a moment and non-zero chiral length scale, Fig. 18. The TIM system $\mathcal{S}_1^{\mathrm{d}}(i = 5)$ exhibits a chiral length scale far exceeding that of the other TIM systems and L_c/h is rather constant throughout the deformation history. In the TIM system $\mathcal{S}_2(i = 6)$ and its dissected variant

20

$\mathcal{S}_2^{\mathrm{d}}(i = 6)$, the moments initially are similar but $\mathcal{S}_2(i = 6)$ retains a more significant chirality throughout the subsequent nonlinear deformation regime. For the hexagon based TIM system, $\mathcal{H}_1(i = 3)$ is achiral, but both dissected variants $\mathcal{H}_1^{\mathrm{d}}(i = 3)$ and $\mathcal{H}_1^{\mathrm{D}}(i = 3)$ are chiral with a significant L_c/h, Fig. 19. For the chiral TIM system $\mathcal{H}_2(i = 3)$ dissection to $\mathcal{H}_2^{\mathrm{d}}(i = 3)$ retains the chirality again and increases L_c/h. Dissection of the TIM systems generally is found to lead to a reduction in axial load-carrying capability. Center-surround dissection leads to TIM system with a larger number of dissected tiles than the center-dissection. Yet, the center-surround dissection leads to a smaller increase in chiral length compared to the center-dissectioned system. The number of dissected tiles has less impact on the chiral length than the distance between the dissected tiles and the loading point.
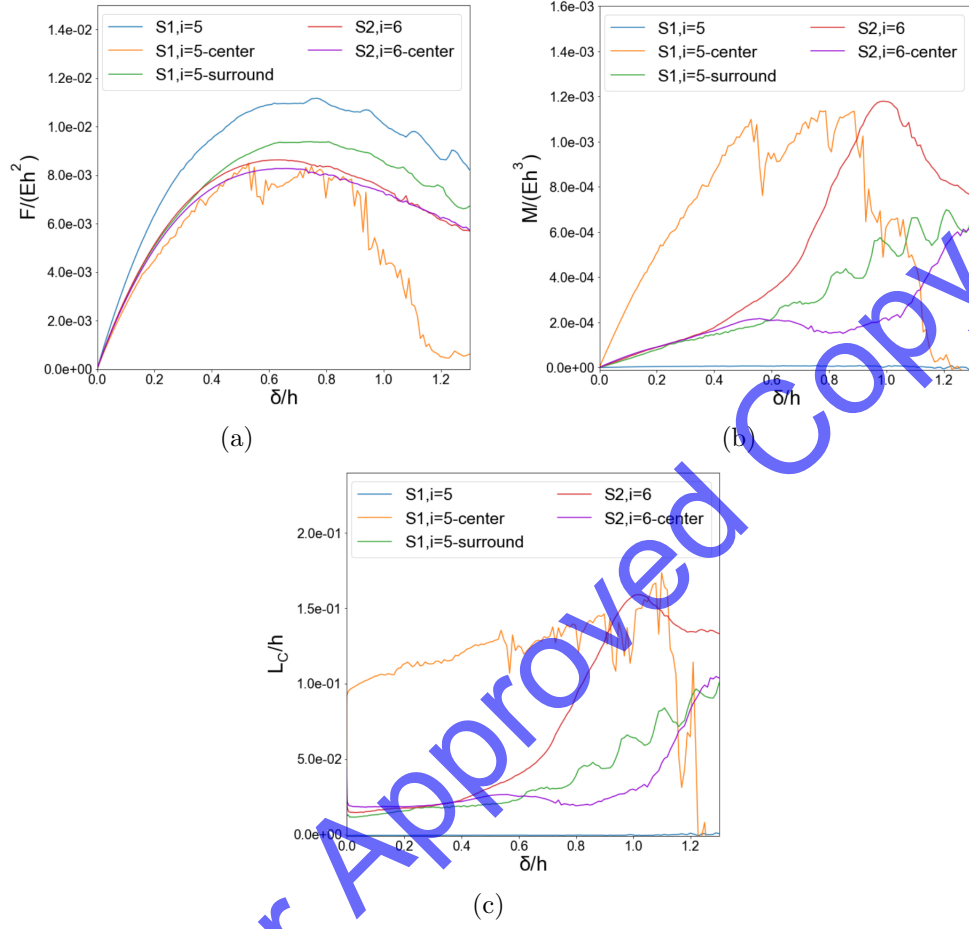
(a)

(b)

(c)

Figure 18: Computational analysis of TIM systems $\mathcal{S}_1(i=5)$, $\mathcal{S}_1^{\mathrm{d}}(i=5)$, $\mathcal{S}_1^{\mathrm{D}}(i=5)$, as well as $\mathcal{S}_2(i=6)$, $\mathcal{S}_2^{\mathrm{d}}(i=6)$. (a) Normalized force, $F/(Eh^2)$, vs. deflection, δ/h, (b) Normalized moment, $M/(Eh^3)$, vs. deflection, δ/h, (c) Normalized chiral length, L_c/h, vs. deflection δ/h.

22

Figure 19: Computational analysis of TIM systems $\mathcal{H}_1(i=3)$, $\mathcal{H}_1^{\mathrm{d}}(i=3)$, $\mathcal{H}_1^{\mathrm{D}}(i=3)$, as well as $\mathcal{H}_2(i=3)$, $\mathcal{H}_2^{\mathrm{d}}(i=3)$. (a) Normalized force, $F/(Eh^2)$, vs. deflection, δ/h, (b) Normalized moment, $M/(Eh^3)$, vs. deflection, δ/h, (c) Normalized chiral length, L_c/h, vs. deflection δ/h.
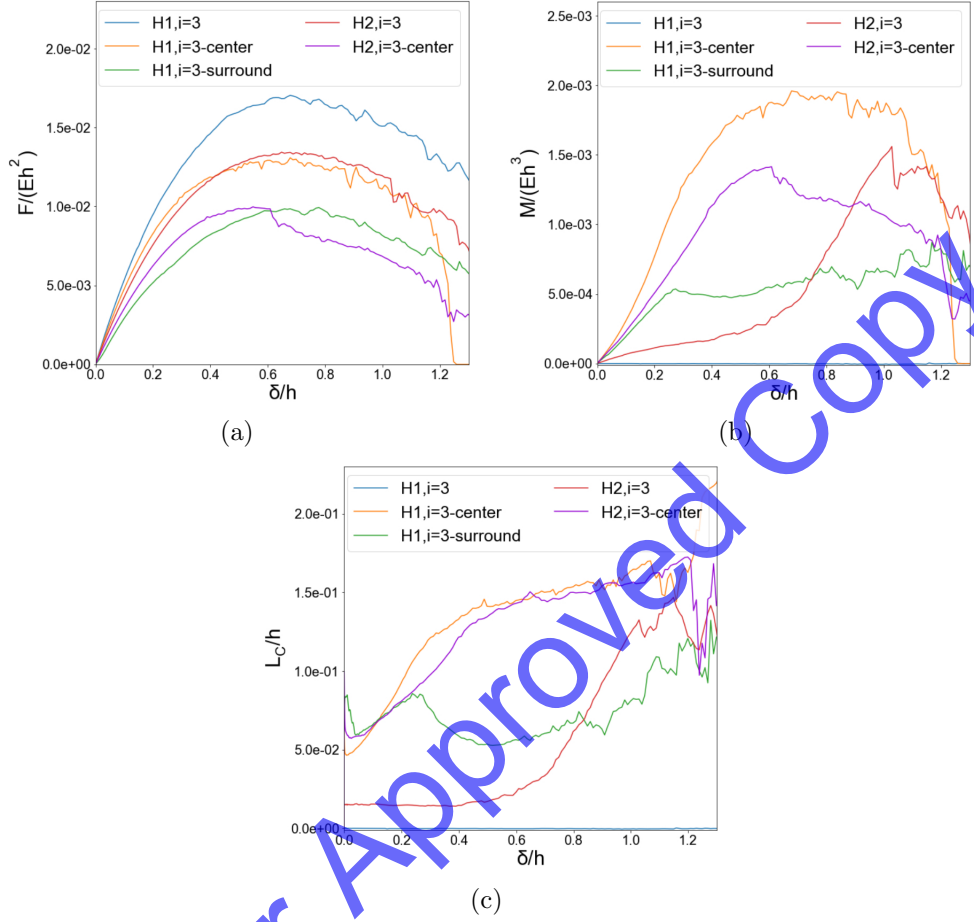
3.3. Experiments

Figure 20 depicts measured transverse force-deflection data and moment-deflection data for TIM systems $\mathcal{S}_1(i=3)$ (achiral), $\mathcal{S}_2(i=4)$ (chiral), $\mathcal{H}_2(i=2)$ (achiral) and $\mathcal{H}_2(i=2)$ (chiral). The data shown are the mean and range for three repeat experiments. Experiments were limited to the magnitudes of deflection $\delta/h < 0.6$ For the achiral systems, $\mathcal{S}_1(i=3)$ and $\mathcal{H}_2(i=2)$ measured moments are of significantly smaller magnitude than those for the chiral systems $\mathcal{S}_2(i=4)$ and $\mathcal{H}_2(i=2)$, respectively. We at-

tribute the non-zero moments for the achiral systems to misalignment in the load system. The behavior of $\mathcal{H}_2(i = 2)$ can be compared to that of its dissected variant, $\mathcal{H}_1^d(i = 3)$, Fig. 21. While for $\mathcal{H}_2(i = 2)$ the moment is small for $\mathcal{H}_1^d(i = 3)$, the moment is significant. Figure 22 summarizes the experiments in terms of the chiral length L_c. The chiral length is found as rather constant throughout the initial, linear stage of deformation but subsequently is found to increase substantially during the nonlinear deformation state.

The general trends observed in the experiments agree well with those from the simulation models. No attempt was made to match the magnitudes of forces and moments, as the focus is on qualitative behavior.
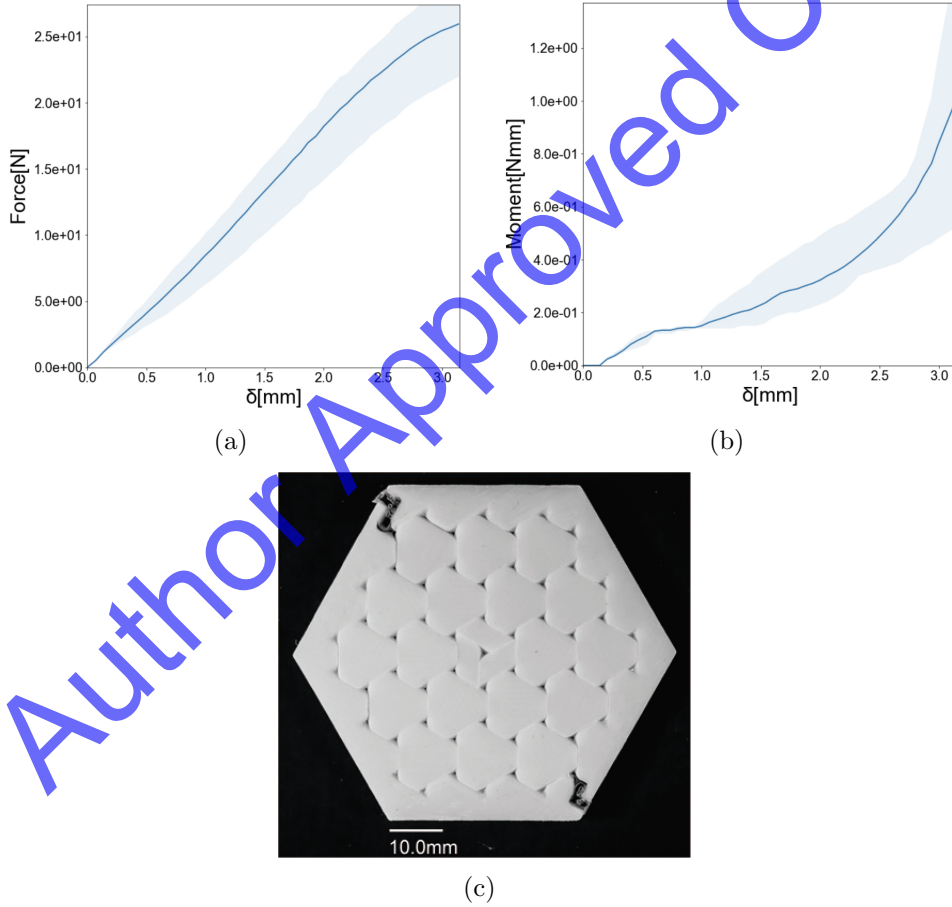

(a)

(b)

(c)

Figure 21: Experimental mechanical properties of hexagon TIM with center dissection. (a) Force F -deflection δ, (b) Moment M -deflection δ, (c) $\mathcal{H}_1^d(i = 3)$.
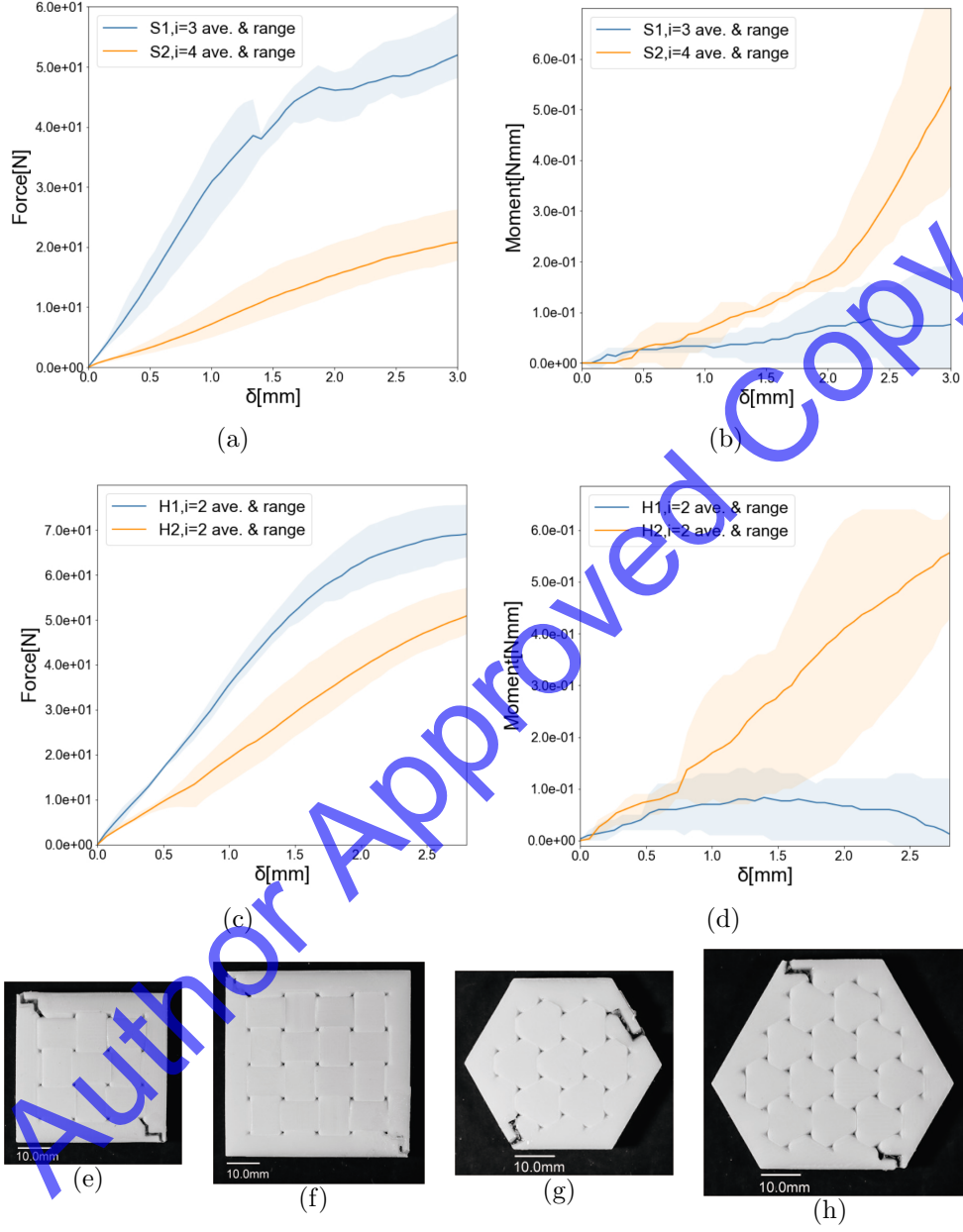
Figure 20: Experiment results present (a) Force, F, vs. deflection, δ, for $\mathcal{S}_1(i = 3)$, $\mathcal{S}_2(i = 4)$, (b) Moment, M, vs. deflection, δ, for $\mathcal{S}_1(i = 3)$, $\mathcal{S}_2(i = 4)$, (c) Force, F, vs. deflection, δ, for $\mathcal{H}_1(i = 2)$, $\mathcal{H}_2(i = 2)$, (d) Moment, M, vs. deflection, δ, for $\mathcal{H}_1(i = 2), \mathcal{H}_2(i = 2)$. (e) $\mathcal{S}_1(i = 3)$ (achiral), (f) $\mathcal{S}_2(i = 4)$ (chiral), (g) $\mathcal{H}_2(i = 2)$ (achiral), (h) $\mathcal{H}_2(i = 2)$ (chiral).
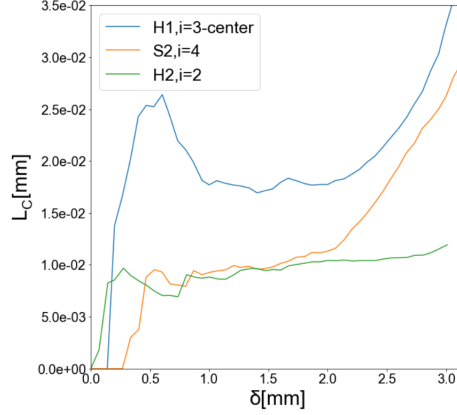
25

Figure 22: Experimental chiral length L_C for $\mathcal{H}_1^{\mathrm{d}}(i=3)$, $\mathcal{S}_2(i=4)$, $\mathcal{H}_2(i=2)$.

4. Discussion

Chirality in the mechanical response of architectured material systems has commonly been found when the unit cells of the chiral material themselves already possess a chiral character, or if the connectors between them impose a chiral structure [35]. [36]. In contrast, in the TIM systems here, individual building blocks as well as the contact and friction interactions between them are non-chiral and the emergence of the overall chiral response is the outcome of the assembly state of the non-chiral building blocks. To effectively represent the interaction between building blocks, a descriptor vector field is utilized and the circulation C of this vector field defines the chirality of the material system architecture. Achiral systems with $C = 0$ do not exhibit a noteworthy reaction moment, while chiral systems generate a significant reaction moment. These concepts apply to both uniform tessellations and dissected tessellations as templates for the construction of TIM systems. Selected experiments qualitatively confirm the computational model results.

For the initial, linear deformation regime, chiral lengths are found to be independent of deformation and system size dependent. The chiral length declines with system size and reaches a steady state at a large system size. A similar size dependence of the chiral length on size was found in [11] for a chiral cellular material. The use of dissections to modify the underlying tessellation at least in the surrounding of the point of load application is a successful strategy to increase the degree of chirality in the linear deformation regime. The TIM system with the most significant degree of chiral response is a dissection of the uniform hexagonal tiling, $\mathcal{H}_1^{\mathrm{d}}(i=3)$, Fig. 12(b).

26

While the bulk of the study focuses on the relationship between chirality and architecture under one loading condition, generalizations of the behavior in the linear response regime are discussed here based on further analysis of the TIM system $\mathcal{H}_1^{\mathrm{d}}(i = 3)$. Two sets of boundary conditions are considered: (1) $\theta_z = 0$, and (2) θ_z free. Analysis results are given in Fig. 23. With $\theta_z = 0$, $M = FL_c$, while for $\theta_z \neq 0$, $M = 0$ and θ_z increases with δ. The mechanical response from can be expressed via Eq. 5, [14]:

$$
\begin{aligned}
F &= C_1\delta + C_2\theta_z \\
M &= C_3\delta + C_4\theta_z
\end{aligned}
\tag{5}
$$

where C_i are the generalized plate stiffness constants, with $C_2 = C_3$. From the case $\theta_z = 0$ and data at $F/(Eh^2) = 1.6 \cdot 10^{-2}$, C_1 and C_3 are obtained as $C_1 = 462.7$ N/mm, $C_3 = C_2 = 126.4$ N. This confirms the relationship $C_3/(C_1h) = L_c/h$. If $\theta_z \neq 0$, no moment is present and θ_z increases with the δ. Now, $C_4 = -C_3(\delta/\theta_z) = -5,938.7$ Nmm. As a result, one can estimate the deflection under a given load in the absence of the rotational constraint as $\delta = (F - C_3\theta_z)/C_1$. In the absence of the rotational constraint, the transverse stiffness is reduced.

The application of cyclic axial loads in combination with changes in boundary condition (switching from constrained to unconstrained during unloading, and back to constrained during loading) can thus be envisioned to create a work cycle similar to those discussed in [37].

We calculate the elastic field and rotational field of the system possessing the highest chiral length at the initial deformation. A difference of around 7% was found between the analytical estimates of Eq. 5 and the full numerical simulations. We attribute this difference to deviation from a fully elastic, reversible response in even the initial stages of deformation.
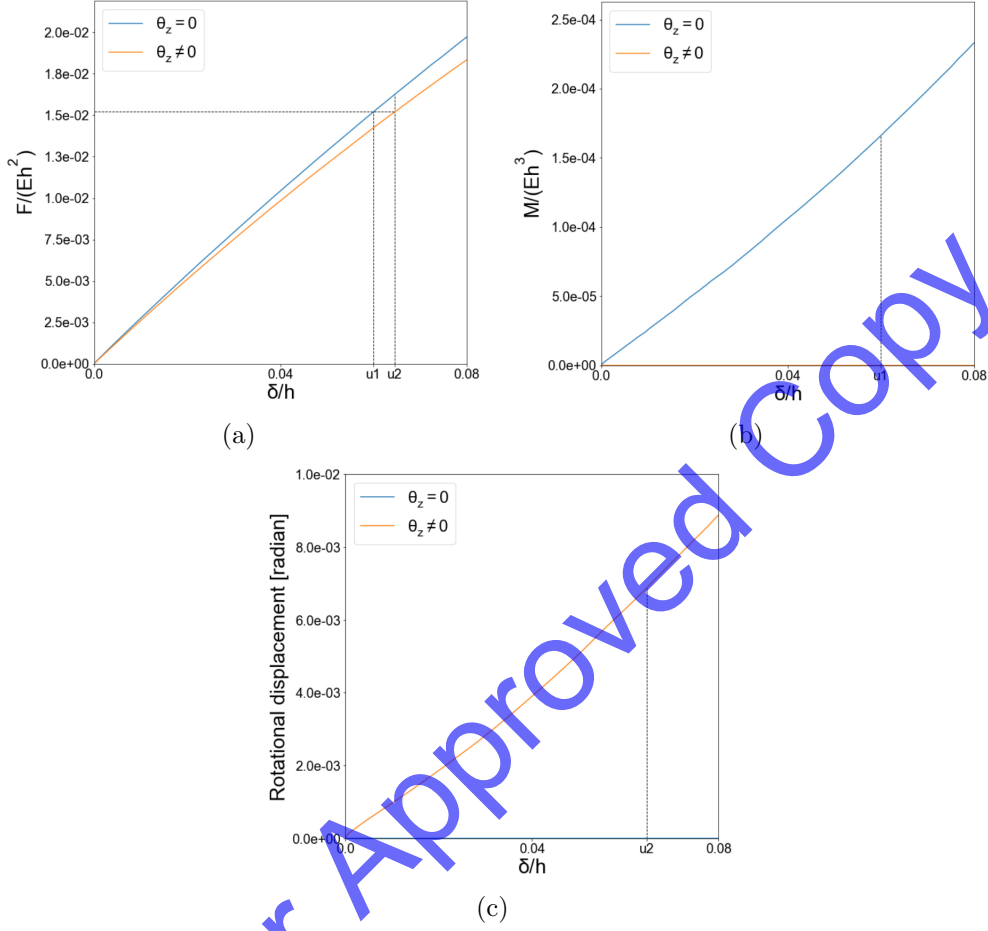
Figure 23: Computational analysis of TIM system $\mathcal{H}_1^{\mathrm{d}}(i=3)$ in the initial linear deformation regime considering the boundary conditions $\theta_z = 0$ and $\theta_z \neq 0$. (a) Normalized force, $F/(Eh^2)$, vs. deflection, δ/h, (b) Normalized moment, $M/(Eh^3)$, vs. deflection, δ/h, (c) Rotation, θ_z, vs. deflection δ/h.

The analysis of chiral mechanical behavior, e.g. Eq. 5 is restricted to the linear elastic regime. With the TIM systems, we can investigate chirality in the nonlinear and damage evolution regime, and thereby investigate the effects of boundary conditions on strength and toughness. As the chiral length scale magnitudes increase in the non-linear deformation regime, more significant effects are expected. Figure 24 depicts the full force-deflection response for the TIM system $\mathcal{H}_1^{\mathrm{d}}(i=3)$ under the boundary conditions $\theta_z = 0$ and $\theta_z \neq 0$. For $\theta_z = 0$ the initial apparent stiffness is higher than for

the unconstraint condition. Strength is predicted as slightly lower in the constrained condition, but deflection to failure is significantly increased in the unconstrained condition. While failure in the constrained condition is more gradual, the unconstrained condition exhibits an increased toughness. Since strength and toughness are now dependent on the boundary conditions, these quantities must be considered as apparent properties in the case of chiral response.
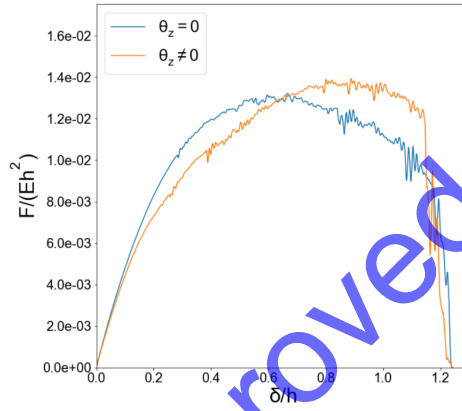

Figure 24: Computational analysis of TIM system $\mathcal{H}_1^{\mathrm{d}}(i = 3)$ considering the boundary conditions $\theta_z = 0$ and $\theta_z \neq 0$, Normalized force, $F/(Eh^2)$, vs. deflection.

5. Conclusion

In topologically interlocked material systems built from achiral building blocks, chirality emerges from the assembly structure. Microstructure modification by introducing dissection is found as an effective approach to further modify the chiral character in TIMs. The combination of building block geometry, tilt vectors, arrangement patterns, and dissection defines a rich array of possible system designs, including achiral and chiral directionality. The TIM system geometry can be described by a vector field, where vectors represent the direction of projection of the tile side walls relative to the assembly plane. The circulation of this vector field is a measure of geometric chirality. If a TIM system is geometrically chiral and possesses a non-zero circulation in the tilt vector field, such a TIM system is mechanically chiral. Beyond the linear regime, the chiral length scale is found to be dependent on deformation and to far exceed that of the elastic regime, indicating a more significant effect of chirality on failure than on elasticity. Two size-effects

29

are found. While mechanical chirality declines with system size in the linear deformation regime, the increase of the chiral characteristics relative to that of the elastic domain increases with system size. In the presence of chirality, strength, deformation to failure and toughness are apparent properties and dependent on the constraint present. A low-constraint configuration exhibits a higher deformation to failure than a high-constraint configuration. This effect is not dissimilar from failure in many ductile metals. Experiments validate key findings from the computational study.

30

References

[1] A. Needleman, A continuum model for void nucleation by inclusion debonding, Journal of Applied Mechanics (1987) 525–531. doi:10.1115/1.3173064.

[2] M. Kuroda, A. Needleman, Non-quadratic strain gradient plasticity theory and size effects in constrained shear, Journal of Applied Mechanics (2023) 1–23. doi:10.1115/1.4062698.

[3] V. Tvergaard, A. Needleman, Nonlocal effects on localization in a void-sheet, International Journal of Solids and Structures 34 (1997) 2221–2238. doi:10.1016/S0020-7683(96)00140-0.

[4] A. Needleman, Computational mechanics at the mesoscale, Acta Materialia 48 (2000) 105–124. doi:10.1016/S1359-6454(99)00290-6.

[5] N. A. Fleck, V. S. Deshpande, M. F. Ashby, Micro-architectured materials: past, present and future, Proceedings of the Royal Society A: Mathematical, Physical and Engineering Sciences 466 (2010) 2495–2516. doi:10.1098/rspa.2010.0215.

[6] L. Yang, O. Harrysson, H. West, D. Cormier, Mechanical properties of 3D re-entrant honeycomb auxetic structures realized via additive manufacturing, International Journal of Solids and Structures 69 (2015) 475–490. doi:10.1016/j.ijsolstr.2015.05.005.

[7] J. N. Grima, A. Alderson, K. Evans, Auxetic behaviour from rotating rigid units, Physica Status Solidi (b) 242 (2005) 561–575. doi:10.1002/pssb.200460376.

[8] A. Spadoni, M. Ruzzene, Elasto-static micropolar behavior of a chiral auxetic lattice, Journal of the Mechanics and Physics of Solids 60 (2012) 156–171. doi:10.1016/j.jmps.2011.09.012.

[9] A. Lorato, P. Innocenti, F. Scarpa, A. Alderson, K. Alderson, K. Zied, N. Ravirala, W. Miller, C. Smith, K. Evans, The transverse elastic properties of chiral honeycombs, Composites Science and Technology 70 (2010) 1057–1063. doi:10.1016/j.compscitech.2009.07.008.

31

[10] L. Meng, J. Shi, C. Yang, T. Gao, Y. Hou, L. Song, D. Gu, J. Zhu, P. Breitkopf, W. Zhang, An emerging class of hyperbolic lattice exhibiting tunable elastic properties and impact absorption through chiral twisting, Extreme Mechanics Letters 40 (2020) 100869. doi:10.1016/j.eml.2020.100869.

[11] T. Frenzel, M. Kadic, M. Wegener, Three-dimensional mechanical metamaterials with a twist, Science 358 (2017) 1072–1074. doi:https://doi.org/10.1126/science.aao4640.

[12] A. Slann, W. White, F. Scarpa, K. Boba, I. Farrow, Cellular plates with auxetic rectangular perforations, physica status solidi (b) 252 (2015) 1533–1539. doi:10.1002/pssb.201451740.

[13] A. Bacigalupo, L. Gambarotta, Chiral two-dimensional periodic blocky materials with elastic interfaces: Auxetic and acoustic properties, Extreme Mechanics Letters 39 (2020) 100769. doi:10.1016/j.eml.2020.100769.

[14] R. Lakes, Elastic and viscoelastic behavior of chiral materials, International Journal of Mechanical Sciences 43 (2001) 1579–1589. doi:10.1016/S0020-7403(00)00100-4.

[15] Z.-L. Zhao, X.-Y. Liu, H. Liu, X.-Q. Feng, J. Yang, Ductility improvement of metallic bars by bioinspired chiral microstructures, Extreme Mechanics Letters 64 (2023) 102063. doi:10.1016/j.eml.2023.102063.

[16] R. Gauthier, W. Jahsman, A quest for micropolar elastic constants, Journal of Applied Mechanics (1975) 369–374. doi:10.1115/1.3423583.

[17] S. Weiner, T. Arad, I. Sabanay, W. Traub, Rotated plywood structure of primary lamellar bone in the rat: orientations of the collagen fibril arrays, Bone 20 (1997) 509–514. doi:10.1016/S8756-3282(97)00053-7.

[18] A. Williams, Load response of topologically interlocked material systems-Archimedean and Laves tilings, Ph.D. thesis, Purdue University Graduate School. Thesis, 2019. doi:10.25394/PGS.8944769.v1.

[19] J. H. Conway, S. Torquato, Packing, tiling, and covering with tetrahedra, Proceedings of the National Academy of Sciences 103 (2006) 10612–10617. doi:10.1073/pnas.0601389103.

[20] M. F. Ashby, Y. J. Bréchet, Designing hybrid materials, Acta materialia 51 (2003) 5801–5821. doi:10.1016/S1359-6454(03)00441-5.

[21] A. V. Dyskin, Y. Estrin, A. J. Kanel-Belov, E. Pasternak, Topological interlocking of platonic solids: A way to new materials and structures, Philosophical Magazine Letters 83 (2003) 197–203. doi:10.1080/0950083031000065226.

[22] T. Siegmund, F. Barthelat, R. Cipra, E. Habtour, J. Riddick, Manufacture and mechanics of topologically interlocked material assemblies, Applied Mechanics Reviews 68 (2016) 040803. doi:10.1115/1.4033967.

[23] M. Short, T. Siegmund, Scaling, growth, and size effects on the mechanical behavior of a topologically interlocking material based on tetrahedra elements, Journal of Applied Mechanics 86 (2019) 111007. doi:10.1115/1.4044025.

[24] M. Mirkhalaf, T. Zhou, F. Barthelat, Simultaneous improvements of strength and toughness in topologically interlocked ceramics, Proceedings of the National Academy of Sciences 115 (2018) 9128–9133. doi:10.1073/pnas.1807272115.

[25] Z. Cheng, M. R. Jones, Assembly of planar chiral superlattices from achiral building blocks, Nature Communications 13 (2022) 1–11. doi:10.1038/s41467-022-31868-2.

[26] S. Bhadra, S. Ghosh, S. Gupta, Emergent chirality and current generation, Physical Review Research 3 (2021) 043179. doi:10.1103/PhysRevResearch.3.043179.

[27] B. Grünbaum, G. C. Shephard, Tilings and patterns, Courier Dover Publications, 1987.

[28] A. Williams, T. Siegmund, Mechanics of topologically interlocked material systems under point load: Archimedean and laves tiling, International Journal of Mechanical Sciences 190 (2021) 106016.

[29] J. Akiyama, K. Matsunaga, Generalization of Haberdasher's puzzle, Discrete & Computational Geometry 58 (2017) 30–50. doi:10.1007/s00454-017-9876-9.

[30] R. Tennant, Dissection methods for aperiodic tilings: From medieval islamic architecture to quasicrystals, in: Conference of the International Journal of Arts and Sciences, volume 7, 2014, pp. 343–348.

[31] N. G. De Bruijn, Algebraic theory of Penrose's non-periodic tilings of the plane., Indagationes Mathematicae 43 (1981) 39–66.

[32] G. N. Frederickson, Geometric dissections now swing and twist, The Mathematical Intelligencer 23 (2001) 9–20. doi:10.1007/BF03026847.

[33] D. Y. Kim, T. Siegmund, Mechanics and design of topologically interlocked irregular quadrilateral tessellations, Materials & Design 212 (2021) 110155. doi:10.1016/j.matdes.2021.110155.

[34] D. Y. Kim, T. H. Siegmund, Abaqus models for chiral tim systems, 2024. URL: https://purr.purdue.edu/publications/4336/1. doi:10.4231/6AT6-RW35.

[35] P. Ziemke, T. Frenzel, M. Wegener, P. Gumbsch, Tailoring the characteristic length scale of 3D chiral mechanical metamaterials, Extreme Mechanics Letters 32 (2019) 100553. doi:10.1016/j.eml.2019.100553.

[36] N. Nejadsadeghi, F. Hild, A. Misra, Parametric experimentation to evaluate chiral bars representative of granular motif, International Journal of Mechanical Sciences 221 (2022) 107184. doi:10.1016/j.ijmecsci.2022.107184.

[37] M. Shaat, H. S. Park, Chiral nonreciprocal elasticity and mechanical activity, Journal of the Mechanics and Physics of Solids 171 (2023) 105163. doi:10.1016/j.jmps.2022.105163.